ELSEVIER

Contents lists available at ScienceDirect

Proceedings of the Combustion Institute

journal homepage: www.elsevier.com/locate/proci





High resolution numerical simulations of methane pool fires using adaptive mesh refinement

Michael A. Meehan a,b,*, John C. Hewson b, Peter E. Hamlington a

- ^a Paul M. Rady Department of Mechanical Engineering, University of Colorado, Boulder, CO 80309, USA
- ^b Sandia National Laboratories, PO Box 5800, Albuquerque, NM 87185, USA

ARTICLE INFO

Keywords:
Pool fires
Buoyant plumes
Adaptive mesh refinement
Transitional flow

ABSTRACT

The ability to accurately predict the structure and dynamics of pool fires using computational simulations is of great interest in a wide variety of applications, including accidental and wildland fires. However, the presence of physical processes spanning a broad range of spatial and temporal scales poses a significant challenge for simulations of such fires, particularly at conditions near the transition between laminar and turbulent flow. In this study, we examine the transition to turbulence in methane pool fires using high-resolution simulations with multi-step finite rate chemistry, where adaptive mesh refinement (AMR) is used to directly resolve small-scale flow phenomena. We perform three simulations of methane pool fires, each with increasing diameter, corresponding to increasing inlet Reynolds and Richardson numbers. As the diameter increases, the flow transitions from organized vortex roll-up via the puffing instability to much more chaotic mixing associated with finger formation along the shear layer and core collapse near the inlet. These effects combine to create additional mixing close to the inlet, thereby enhancing fuel consumption and causing more rapid acceleration of the fluid above the pool. We also make comparisons between the transition to turbulence and core collapse in the present pool fires and in inert helium plumes, which are often used as surrogates for the study of buoyant reacting flows.

1. Introduction

Accurately predicting and understanding the structure and dynamics of pool fires is of great interest in a wide variety of applications. In accident scenarios, unplanned releases of liquid fuel can, for example, produce unexpected self-sustaining flames. Without proper risk mitigation, the ensuing flames can damage nearby materials and possibly promote rapid flame propagation, leading to catastrophic events. In wildland fires, solid material scattered throughout forests acts as a fuel source and, in many cases, the resulting fires are similar to liquid pool fires due to the importance of buoyancy effects in driving both flows.

Many researchers have focused on improving predictive capabilities for pool fires [1] with a primary emphasis on constructing empirical relationships and validating computational simulations against available experimental data [2–4]. However, simulations of pool fires are made challenging by the presence and coupling of various physical processes spanning wide spatial and temporal scale ranges. These processes include buoyancy-generated turbulence [5,6], small-to-large scale kinetic energy transfer [7], heat transfer due to gas-phase combustion [8], and soot and radiative transport [9].

In addition to these processes, many pool fires include both laminar and turbulent regions, leading to potentially large variations in mixing and HRR. This dual behavior is exemplified by the fact that, even for laminar conditions, pool fires exhibit large-scale vortex shedding at a scale equivalent to the pool diameter (i.e., associated with the puffing instability). At the same time, when the local Reynolds number becomes sufficiently large, viscous dissipation occurs at increasingly fine scales [10]. The resulting scale separation poses challenges for coarse simulations with subgrid-scale (SGS) models of unresolved phenomena, as in Reynolds-averaged Navier-Stokes (RANS) approaches or large eddy simulations (LES). Many SGS models rely on large Reynolds number arguments and the net downward cascade of kinetic energy, neither of which are generally applicable for all pool fire conditions and regions. As a result, accurate modeling of pool fires typically requires finely-resolved LES [9,11] to reduce the reliance on SGS models, but even then, most such models still do not account for known physical processes in buoyancy-driven flows, such as up-scale energy transfer [7, 10]. Limitations of the LES approach have been demonstrated from the MaCFP workshop where the best modeling approaches have difficulty matching second-order statistics against experimental data [1,12].

^{*} Corresponding author at: Sandia National Laboratories, PO Box 5800, Albuquerque, NM 87185, USA. E-mail address: mameeha@sandia.gov (M.A. Meehan).

In this study, we simulate methane pool fires using adaptive mesh refinement (AMR) to directly resolve small-scale flow features. By taking this approach, we can avoid using SGS models, which are known to perform poorly during the laminar-to-turbulent transition that typically occurs at the inlet [6]. The computational savings and fine resolutions enabled by the use of AMR further allow us to more accurately represent chemical processes by directly solving finite-rate chemical kinetics equations, as opposed to using flamelet, progress variable, or eddy dissipation concept approaches [9]. Although AMR has been used extensively in other turbulent combustion problems (e.g., statistically stationary one-dimensional flames [13] and laboratory-scale slot burners [14]), it is still quite new to simulations of plumes [10,15] and fires [16]. Moreover, due to the AMR, the present study is the one of the first to perform numerical simulations of turbulent pool fires with detailed chemistry [17].

Here we perform simulations of three different methane pool sizes to understand fire dynamics as the flow transitions from laminar to turbulent. By simply increasing the pool size, the near-field puffing instability undergoes a transition to turbulence, which would normally be difficult to model accurately using traditional modeling approaches. From the simulations, we examine how first-order statistics and streamwise fluxes are affected as mixing is enhanced by the onset of Kelvin–Helmholtz fingering and core collapse. We then compare the present simulations with the helium plumes of Meehan et al. [18,19] in an effort to align the parameters that dictate when inert and reacting plumes undergo transition to turbulence; this is particularly important, for example, since some lower-fidelity modeling approaches could incorporate this transition in turbulence models for LES [20].

The remaining text is organized as follows. A summary of the numerical simulations is provided in Section 2. Visualizations and statistics of the fires are presented in Section 3. In Section 4, we discuss how to recast the parameters dictating transition to turbulence in inert helium plumes for application to the present reacting plumes. In Section 5, we highlight conclusions and important directions for future work.

2. Numerical simulations

We simulate methane pool fires by solving the three-dimensional (3D) low-Mach multi-species reactive Navier–Stokes equations using PeleLMeX [21], an exascale hydrodynamics code built on AMReX, a software framework for block-structured AMR [22]. PeleLMeX is a second-order accurate (in space and time) finite volume code. We took advantage of the highly-scalable infrastructure incorporated into PeleLMeX to simulate the plumes across 165 nodes using Department of Defense computing resources. In total, 40–50 million CPU hours were required to perform the simulations shown herein.

The governing equations and numerical calculations are discussed in the publicly available code repository [21]. The only difference in the present simulations, as compared to the public code, is the inclusion of buoyancy effects here. This results in an additional term, $(\rho - \rho_{\infty})g_i$, on the right hand side of the momentum equation, where ρ is the local fluid density, ρ_{∞} is the density of the ambient air, and g_i is the gravitational acceleration. Chemical reactions are modeled using DRM-19, a multi-step mechanism with 20 species and 84 reactions that has been reduced from the full GRI 1.2 mechanism [23]. The mechanism has been shown previously [24] to provide a good balance of fidelity and computational cost.

The pool fires are modeled in cubic computational domains of size $(6D)^3$ where D is the diameter of the circular pool through which methane is injected. We consider three different pool diameters: D=6.25 cm, 12.5 cm, and 25.0 cm, which we will refer to as D1, D2, and D3, respectively. A summary of the simulations is provided in Table 1. In each simulation, we used an underlying base mesh of 256^3 and refined up to three additional levels using AMR up to a height

of z/D = 4, where z is the vertical coordinate extending perpendicularly upward from the pool. The grid is refined during the AMR procedure based on cell-to-cell density differences and heat release rate (HRR). Visualization of the AMR is provided in the first column of Fig. 1. With AMR, the resulting finest grid resolution was 0.73 mm. Overall grid cell counts in the simulations ranged from roughly 25 million for the smallest case to 100 million for the largest case. It is important to note that we consider the resolution of 0.73 mm to be well-resolved but do not consider this to be equivalent to direct numerical simulations (DNS). The present simulations do not resolve all of the scales extending into the dissipation range and full flame physics, where we would expect resolutions on the order of 0.1 mm to be necessary [25]. Rather, the present simulations capture largescale mean and global quantities necessary to support the conclusions herein. At the smallest scales, numerical dissipation acts as a form of effective eddy viscosity [26], relieving the need for an explicit SGS model. Our previous work [18] indicated a resolution of approximately 2 mm was sufficient for convergence of mean and fluctuating quantities (e.g., root-mean-square of velocity fluctuations, puffing frequency) for inert plumes of similar buoyancy characteristics. Additional resolution was required, however, for convergence of higher-order gradient terms (e.g., enstrophy budgets). The increase in viscosity due to combustion for the present simulations is only expected to lower the local Reynolds number and support the sufficiency of 0.73 mm.

The presence of the flame introduces a new scale compared to the inert helium plumes that needs to be sufficiently well-resolved in order to capture the appropriate buoyant production in the pool fire. The integrated HRR may be regarded as a representative quantity. We conducted three additional simulations (not shown here) of D1 with double the height of the computational domain to ensure no methane was convected out of the domain. The finest resolution of the three simulations was 1.5 mm, 0.73 mm, and 0.37 mm. The respective average integrated HRR were calculated as 2.61 kW, 2.99 kW, and 3.04 kW, indicating the flame is well-resolved using the present 0.73 mm of resolution. Furthermore, we performed corresponding simulations of one-dimensional counterflow diffusion flames in Cantera and found the peak HRR spanned 2 – 4 mm, roughly equivalent to 3 – 6 fine grid cells. Instantaneous flame normal profiles from the present simulations found a similar number of cells spanned the peak HRR.

In the simulations, methane is injected into quiescent air through a round inlet at the bottom of the domain at velocity $U_0 = 2$ cm/s, and both the initial methane and air temperatures, T_0 and T_{∞} , respectively, are set to 300 K. The inlet is modeled as a Dirichlet boundary condition with pure methane transitioned to pure air at the inlet edge according to a hyperbolic tangent profile [18]. A Dirichlet boundary condition is preferred here over a convective/diffusive boundary condition to better compare with simulations performed by Meehan et al. [18] in Section 4, but the development of turbulence is expected to be similar between the different boundary conditions. The ambient pressure is atmospheric with an imposed hydrostatic pressure gradient as a result of the gravitational field, with $g_z = -g$, where g = 9.81 m/s² is the magnitude of the gravitational acceleration. The remaining five boundary conditions are modeled as open Neumann boundaries, allowing air to freely be entrained or combustion products to exit the domain. The non-dimensional Froude, Richardson, and Reynolds numbers based on inlet conditions are provided in Table 1 for each of the cases and are defined, respectively, as $Fr_0 = U_0/(gD)^{1/2}$, $Ri_0 = (1 - \rho_0/\rho_\infty)gD/U_0^2$, and $Re_0 = \rho_0 U_0 D/\mu_0$, where ρ_0 and μ_0 are the density and viscosity of methane. These cases are designed to span a range of turbulence conditions, from laminar, to transitional, to fully turbulent flow.

To reach a statistically stationary state, we initially injected methane at $300~\rm K$ for approximately $0.1~\rm s$. We then rapidly increased the methane temperature at the inlet to $2400~\rm K$ for $0.2~\rm s$ to ignite the pool fire, then dropped the temperature back to $300~\rm K$. This procedure allows the methane and air to mix, ignite, then produce a self-sustaining flame. After this procedure, we allowed the flame to continue to develop for $2{\text -}3~\rm s$ before beginning data collection for analysis. The total amount of simulation time analyzed in each case is provided in Table 1.

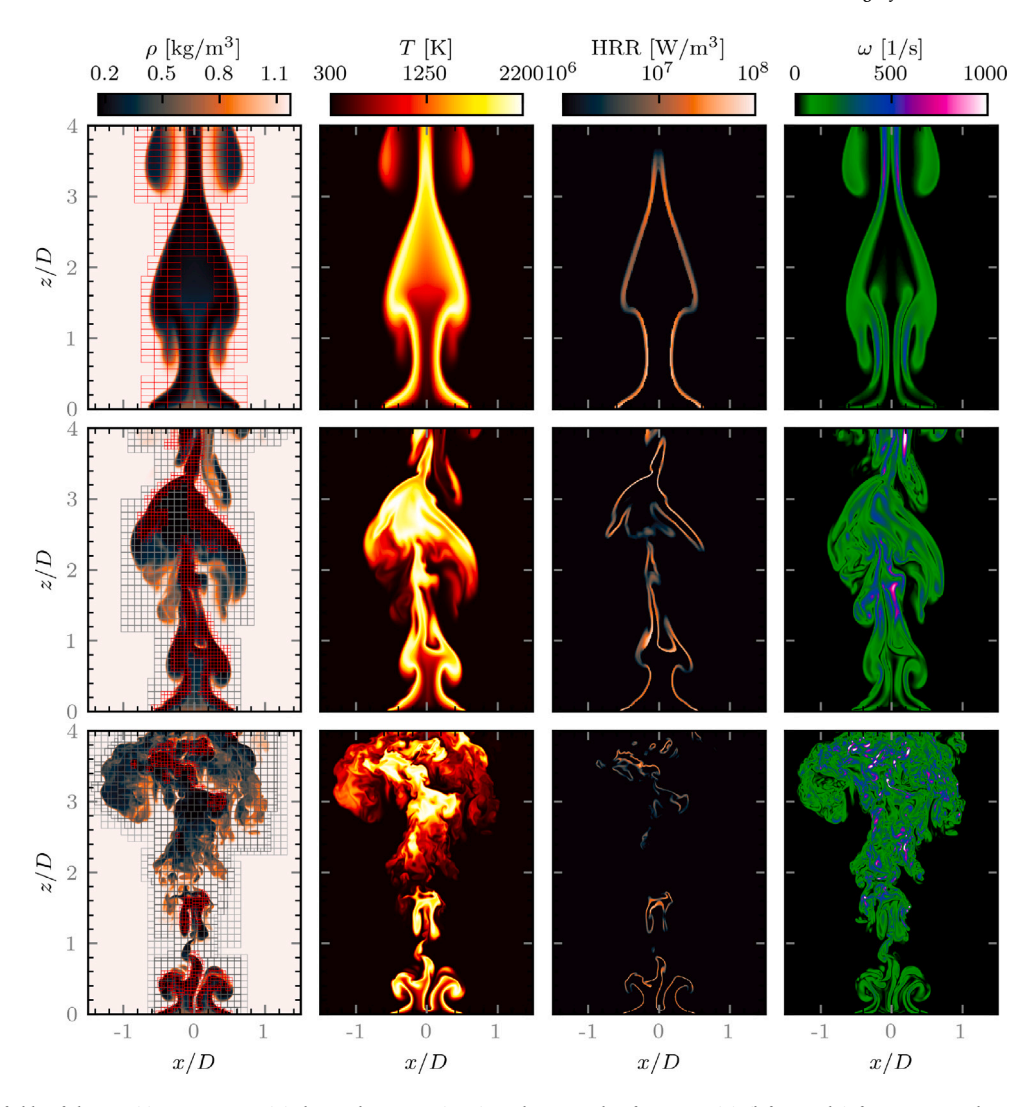


Fig. 1. Instantaneous fields of density (ρ), temperature (T), heat release rate (HRR), and magnitude of vorticity (ω) (left to right) for D1, D2, and D3 at the y/D=0 plane. The first column also shows the locations of finest AMR levels in red and intermediate AMR levels in gray (note that the boxes represent AMR levels and do not show the grid itself, which is much finer). (For interpretation of the references to color in this figure legend, the reader is referred to the web version of this article.)

Table 1
Physical and simulation parameters for the three methane pool fire simulations performed in the present study.

Simulation	Diameter (D)	Fr_0	Ri_0	Re_0	Domain size	AMR Levels	Sim. time	Est. CPU
D1	0.0625 m	0.0255	680	71.1	$(0.375 \text{ m})^3$	1	15.0 s	2.5 m h
D2	0.125 m	0.0181	1360	142.2	$(0.75 \text{ m})^3$	2	10.0 s	8.4 m h
D3	0.25 m	0.0128	2721	284.5	$(1.5 \text{ m})^3$	3	7.0 s	35 m h

3. Results

Fig. 1 shows instantaneous fields of ρ , T, heat release rate (HRR), and vorticity magnitude, $\omega=(\omega_i\omega_i)^{1/2}$ where ω_i is the vorticity vector, for D1, D2, and D3. Qualitatively, these fields show that as the diameter increases, the flow transitions from laminar to turbulent. The smallest diameter pool, in case D1, has highly organized spatial structures that are symmetric about the x axis. For D2, the vortex shedding structure is still quite organized for $z/D \le 1$ but does not exhibit the same symmetry as seen in D1. For larger z/D, the flow becomes more chaotic with the formation of smaller scale irregular features. Lastly, the fields for D3 show the effects of air penetrating downward towards the inlet, where we see increased temperature and HRR at the base of the pool fire near the inlet. This penetration is associated with core collapse at the inlet [9] and leads to changes in the puffing behavior of the flow [19].

3.1. Puffing instability

The puffing instability is a global instability that forms due to rapid buoyancy-driven acceleration of low density fluid into higher density fluid, producing large-scale vortical structures [29]. Early experimental research on axisymmetric reacting pool fires found that there is a strong correlation between the pool diameter and oscillation frequency, f, which can be expressed as $f=0.48\,(g/D)^{1/2}$ [27]. This relation was later written in non-dimensional form as [28]

$$St = 0.48Fr_0^{-1}$$
, (1)

where $\mathrm{St} = f D/U_0$ is the puffing Strouhal number. An important characteristic of the scaling relationship in Eq. (1) is its robustness through the transition to turbulence. Moreover, non-dimensional parameters beyond Fr_0 seem to have either a small or negligible effect on St , including the Reynolds number [18].

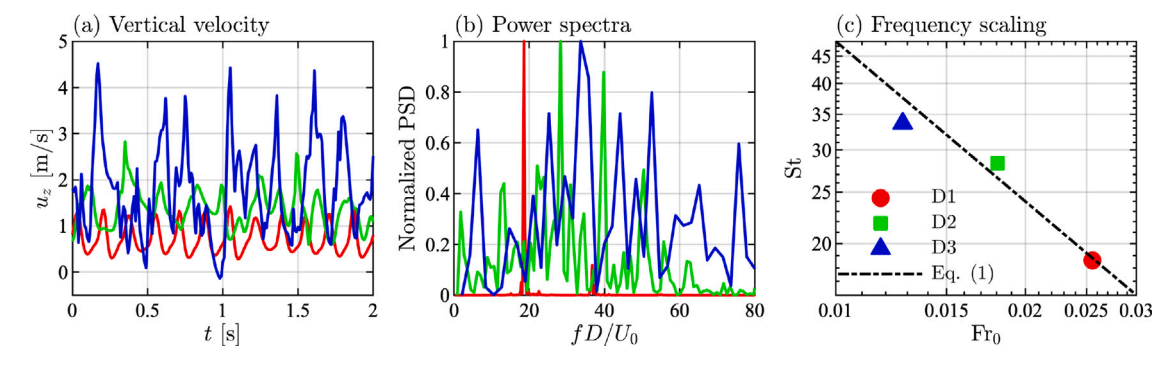


Fig. 2. Temporal properties of cases D1, D2, and D3 from (a) time series of vertical velocity u_z at z/D=0.5 along the centerline, (b) power spectral densities of the signals in (a) normalized by the peak magnitude, and (c) computed St for the present cases compared against the relation in Eq. (1) [27,28].

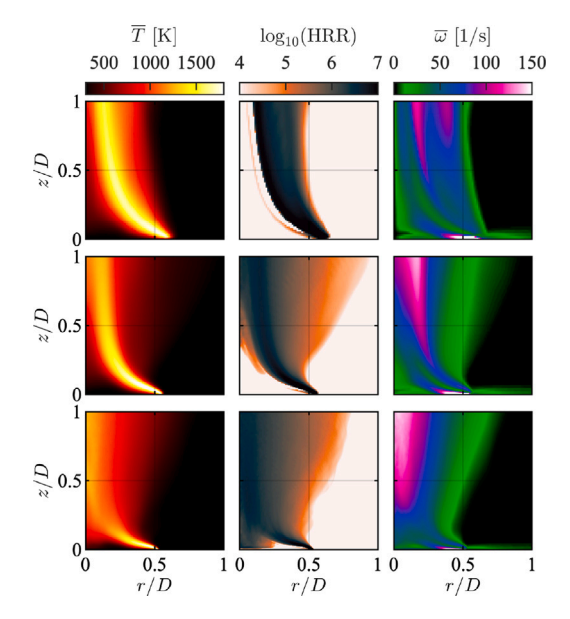


Fig. 3. Time and azimuthal averages of \overline{T} (left column), $\log_{10}(\overline{HRR})$ (center column), and $\overline{\omega}$ (right column) for D1 (top row), D2 (middle row), and D3 (bottom row), where $\overline{(\cdot)}$ is a time and azimuthal average.

To evaluate St in the present simulations, we extracted a time series of the vertical velocity (u_z) at z/D=0.5 along the centerline (i.e., for x/D=y/D=0); Fig. 2(a) shows segments of the resulting time series for D1, D2, and D3. Using the full time series, we computed the power spectral densities shown in Fig. 2(b) and compare the peak frequencies with the experimental relation from Eq. (1) in Fig. 2(c). Fig. 2(a) shows very regular puffing cycles for D1 that become more erratic as D increases (i.e., in D2 and D3). Overall, Fig. 2(c) shows that the puffing frequencies computed here agree well with Eq. (1), providing validation of the AMR approach for the present pool fires.

3.2. Azimuthal averages

The temporal and azimuthal averages of T, HRR, and ω shown in Fig. 3 reveal further substantial differences between the different pool fire cases. There is a broadening of the region over which the average temperature is elevated as the pool diameter increases. Concentrations of increased temperature are located in the shear layer region along the fuel-air mixing region. This region can be easily identified for the entire vertical region shown for D1 and D2; however, D3 only shows this for a very confined region near the pool surface. This is a result of the turbulent eddies penetrating into the core of the plume, often referred to core collapse [9] or Rayleigh–Taylor spikes [18,19]. For inert plumes, this simply corresponds to increased mixing rates

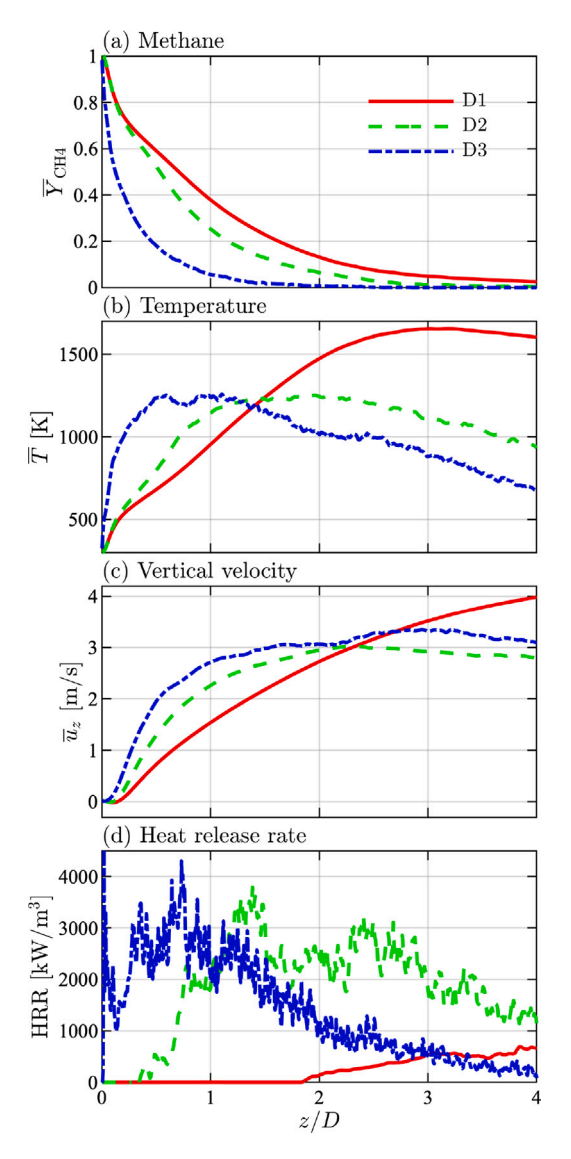


Fig. 4. Temporal averages of (a) methane mass fraction, (b) temperature, (c) vertical velocity, and (d) heat release rate per unit volume along the centerline (i.e., at x/D = y/D = 0) as a function of height above the pool inlet (z/D) for cases D1, D2, and D3.

downstream. For reacting plumes, core collapse results in increased mixing of fuel and oxidizer, allowing for increased overall reaction rates. This consequence can be seen in the average HRR fields in Fig. 3, where there is increasingly large HRR along the centerline and near the

inlet as the diameter increases. Spatially-integrated values of HRR over the entire domain yield values of 2.7 kW, 10.6 kW, and 39.8 kW for D1, D2, and D3, respectively.

The average vorticity magnitude fields in Fig. 3 highlight two important features of pool fires. First, when the flow is laminar or transitional, the maximum vorticity is confined to the shear layer region at the edge of the pool fire. For the turbulent pool fire (i.e., D3), however, the maximum vorticity is primarily controlled by small-scale turbulent fluctuations, which primarily occur along the centerline; this can also be seen in the fields shown in Fig. 1. Second, there are very large concentrations of vorticity near the pool surface where there is rapid flow contraction. With increasing diameter, this region becomes more confined to the pool surface. When considering pool fires where the fuel surface is a liquid, there will be very strong coupling between the gas and liquid phases [8]. Modeling this behavior using a wall-modeled approach in RANS or LES would likely be very challenging using standard approaches, particularly in the presence of other factors like wind [11].

3.3. Centerline profiles

As shown in Section 3.2, a consequence of the increased mixing along the centerline is that there is an increase in burning near the base of the pool fire. To emphasize this further, we show the average temperature, methane mass fraction, vertical velocity, and HRR along the centerline (i.e., x/D = y/D = 0) for all three pool diameters in Fig. 4.

As the pool diameter increases, Fig. 4(a) shows that methane is consumed more quickly as a function of downstream distance. This is a consequence of the increased pool size leading to more chaotic conditions, resulting in increased mixing and chemical reactions. Similarly, temperature in Fig. 4(b) increases more rapidly near the base of the plume. With increased temperatures in the combustion products, there is a stronger buoyant force that accelerates the fluid upwards, as can be seen with increases in \bar{u}_z near the base of the plume. Additionally, while there is no unified framework to determine flame height from simulations (unlike experiments which typically use intermittency [30]), a flame height could be estimated from temperature contours [11] or diminished HRR [31]. Using $\bar{T}\approx 1000$ K, the flame height may be estimated for D3 as $z/D\approx 2.6$ for D3. This value is substantiated by the HRR decreasing at this height and is consistent with predictions using correlations from Heskestad [32].

This observation of increasing centerline vertical velocity with increasing diameter is in contrast to the findings of [19] for inert helium plumes. In [19], the observation of core collapse resulted in *decreased* velocity near the pool surface because this additional mixing increased the local density and the Rayleigh–Taylor spikes were able to penetrate downward into the core. For pool fires, mixing from the downward (air) spikes accelerates heat release, providing negative feedback to the development of vertical velocity. Therefore, we expect there to be a transition for a given fuel composition that results in a balance between the downward momentum of the spikes and the increase in buoyancy due to reactions.

3.4. Vertical fluxes

Integral models derived from the Navier–Stokes equations are valuable in approximating first-order global statistics (e.g., mass entrainment, flame height, etc.) in buoyancy-controlled fires [33]. Typically, these models are developed by considering a control volume and integrating across the relevant surfaces, forming a system of equations of significantly lower dimension that can be used to provide reasonable estimates of flow properties or to enable more efficient parameter space explorations.

To inform the development of these integral models when considering the laminar to turbulent transition, we compute the buoyancy and mass fluxes \mathcal{B} and \mathcal{M} , respectively, for the present simulations and

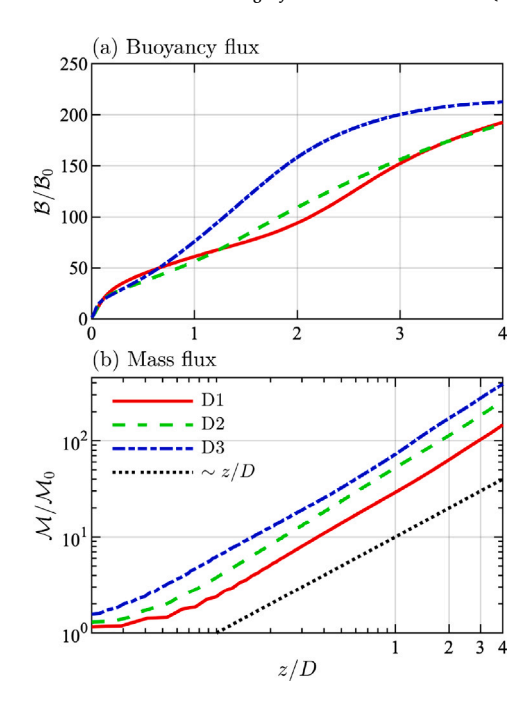


Fig. 5. Computed values of the (a) buoyancy flux B from Eq. (2) and (b) mass flux M from Eq. (3) as functions of vertical distance above the pool inlet (z/D). The fluxes are normalized by their respective inlet values B_0 and M_0 , and the mass entrainment scaling relationship $M/M_0 \sim z/D$ from Delichatsios [33] is shown in (b).

show them normalized by their inflow values as a function of vertical direction z/D in Fig. 5. These fluxes are defined as

$$B(z) = g \int_0^\infty (\rho_\infty \overline{u}_z - \overline{\rho} u_z) 2\pi r \, dr, \qquad (2)$$

$$\mathcal{M}(z) = \int_0^\infty \overline{\rho u_z} 2\pi r \, \mathrm{d}r, \tag{3}$$

where $\overline{(\cdot)}$ denotes a time and azimuthal average. Fig. 5(a) shows that although there are significant increases in burning near the inflow, there is no resulting difference in $\mathcal{B}/\mathcal{B}_0$ until approximately $z/D \approx 1$. Beyond $z/D \approx 1$, $\mathcal{B}/\mathcal{B}_0$ for D3 is slightly larger than that of D1 and D2, but near $z/D \approx 4$, $\mathcal{B}/\mathcal{B}_0$ is similar in all cases. This difference is almost entirely due to differences in fuel consumption rates. That is, \mathcal{B} begins to level off for D3 because most of the methane has been burned while D1 and D2 still have methane present in the flow (as shown in Fig. 4). Since the total buoyant flux is proportional to the fuel flux, or \mathcal{B}_0 , the rate of buoyancy generated is increased by core collapse (observed in D3) in the region between $z/D \approx 1-4$. Future work is required to determine whether radiation and soot in transitional regimes will affect this result.

The mass fluxes in Fig. 5(b) are also sensitive to the transition to turbulence. Once the linear scaling relationship develops near $z/D \approx 0.1$, a consistent discrepancy between the three simulations is observed. This indicates that the structure of the vortex roll-up near the base of the plume causes variability in the amount of air entrained, although the rate of entrainment, $d(\mathcal{M}/\mathcal{M}_0)/d(z/D)$, is relatively constant beyond $z/D \approx 0.1$. An important note is that the discrepancy is not solely dictated by the presence of core collapse since there is also a discrepancy between D1 and D2 where core collapse is not observed.

4. Discussion

The results in Section 3 show that as the diameter of the pool increases, the flow transitions from laminar to turbulent with increasing inlet Reynolds (Re_0) and Richardson (Ri_0) numbers. However, the introduction of chemical reactions adds ambiguity when defining

appropriate controlling parameters, since the inlet properties are no longer representative of the source of buoyancy (i.e., hot combustion products) in pool fires.

As a result, here we seek alternative Richardson and Reynolds number definitions that are more directly connected to the source of buoyancy in pool fires, but that also allow comparisons with transitional values of Re_0 and Ri_0 in inert plumes (for example those identified in Ref. [18]). Being able to consistently predict these transitional values is extremely important in terms of modeling pool fires because (i) insufficient resolution of the numerical grid will suppress this vortex breakdown mechanism [10], (ii) the production mechanisms associated with kinetic energy and enstrophy can change substantially, and (iii) low-fidelity modeling may need to account for changes in subgrid processes [20]. A comparison between inert and reacting plumes to understand transition to turbulence has not been done before.

Here we propose Reynolds and Richardson numbers with dimensional parameters more pertinent to reacting plumes. First, a natural substitution of the inlet density (ρ_0) would be ρ_f , the density of hot products with temperature T_f resulting from an adiabatic, stoichiometric reaction. Because the puffing instability is driven by buoyancy, ρ_f would be the most buoyant local density of the flow. It should be noted that any reasonable replacement of ρ_0 will only modestly affect Ri, since ρ_{∞} is usually much larger than ρ_f , making $(1 - \rho_f/\rho_{\infty})$ nearly always close to unity. Next, we maintain the pool diameter D as the relevant length scale since, for both inert and reacting plumes, the puffing vortices are of comparable size, particularly in the laminar and transitional regimes, independent of whether the plume is reacting or not. We replace U_0 with U_f , the flame speed of the stoichiometric mixture. This seems most appropriate since in reacting plumes, $U_f \gg$ U_0 and this is the velocity most relevant in the shear layer prior to the acceleration by buoyancy. Lastly, we continue the use of μ_0 , the viscosity of the fuel. This can be justified by noting that the primary reason for the plume to transition to turbulence is due to the presence of core collapse, and since core collapse occurs just above the inflow, μ_0 should be more appropriate than μ_f in defining the most relevant local fluid viscosity.

From these arguments, we propose two new definitions of Richardson and Reynolds numbers that allow transition in the present cases to be compared directly with inert helium plumes:

$$\operatorname{Ri}_{f} = \left(1 - \frac{\rho_{f}}{\rho_{\infty}}\right) \frac{gD}{U_{f}^{2}},\tag{4}$$

$$Re_f = \frac{\rho_f U_f D}{\mu_0} \,. \tag{5}$$

These formulations yield the values of Ri_f and Re_f provided in Table 2 for the present cases.

We compare these with the values of the helium plumes from Meehan et al. [18]. Based on the analysis in Section 3, D1 was found to be laminar because there was no core collapse and a single peak was found in the PSD of puffing frequency. The middle case, D2, is considered transitional since there is no core collapse but the spectrum was much broader. Finally, D3 is turbulent since core collapse causes very chaotic motion at the base of the plume. Comparing the corresponding values of Ri_f and Re_f directly to Meehan et al. [18] yields an identical classification of the plumes. For example, $\mathrm{Ri}_f=3.2$ for D1, which is near the lowest value of Ri_0 studied in Meehan et al. [18], but the value of Re_f for D1 is below the critical Re_0 value from [18] where the flow switches from laminar to transitional. Hence, D1 could have been anticipated to be laminar by computing Ri_f and Re_f and comparing directly to the inert helium plumes.

There are a number of important consequences of this result in terms of SGS modeling. In both RANS and LES, *a priori* knowledge of the transition point is necessary to adjust the SGS modeling approach [34]. The present analysis would minimize the required number of simulations of reacting plumes to build these empirical correlations, and instead leverage knowledge of transition in inert plumes. Even a

Table 2 Values of Ri_f and Re_f from Eqs. (4) and (5), respectively, for the present cases. The type of flow indicated here is determined by comparing Ri_f and Re_f to the values of Ri_0 and Re_0 for the inert plumes of Meehan *et al.* [18].

Simulation	Ri_f	Re_f	Type
D1	3.2	335	Laminar
D2	6.4	671	Transitional
D3	12.8	1342	Turbulent

dynamic procedure for LES modeling may need to consider this supplementary information despite zero turbulent viscosity in the laminar regions [35]. Exploring how SGS modeling is related between reacting and inert plumes is left as future work.

5. Conclusions and future work

In the present study, we conducted three high-resolution 3D numerical simulations of gaseous methane pool fires with different diameters to study how the flow dynamics change as the pool fire changes from laminar to turbulent. To ensure that small-scale structures were well-resolved, we used adaptive mesh refinement to dynamically refine the mesh where chemical reactions and strong vortices were present.

Through a detailed analysis of the resulting pool fires, we showed that the flow was distinctly laminar, transitional, and turbulent for the smallest, middle, and largest diameter pools, respectively. The analysis showed that when core collapse is present in the turbulent plume, there is an increase in vertical velocity just above the pool surface relative to laminar or transitional puffing instability despite the presence of downward penetration of ambient air; this is contrary to what was found for helium plumes [19]. Additionally, transition to turbulence was found to impact the near-field buoyancy flux and rate of fuel consumption, and also significantly impacted the entrainment of the air very close to the pool surface. Finally, we made direct comparisons of the present reacting plumes to the inert plumes of [18] through the formulation of relevant non-dimensional numbers to help predict when pool fires will transition to turbulence.

While the present results were enlightening in terms of better understanding the transition to turbulence, significantly more work needs to be done. In the future, we would like to perform additional simulations that include more detailed physics and geometric representations of the pool fires (e.g., radiation, boundary surfaces, etc.). We would also like to use these simulations for further physical analysis of integral equations for flux estimates and small-scale quantities to improve subgrid-scale modeling. Specifically, these simulations could be used to inspect errors associated with classic subgrid combustion or turbulence models, such as flamelets [9]. Further physical analysis of the kinetic energy dynamics may suggest novel SGS models need to incorporate known features of buoyant flows, such as upscale energy transfer and anisotropic small scales [6,10].

Novelty and significance statement

This study outlines one of the first set of pool fire simulations that directly resolve small-scale processes, including finite-rate multistep chemistry and resolved, rather than modeled, small-scale turbulent mixing. This is accomplished through the use of adaptive mesh refinement which allows us to refine localized regions of the flow where significant chemical reactions and turbulent structures are present. Based on an analysis of the resulting simulations, we demonstrate how the transition to turbulence in pool fires affects major statistics such as centerline profiles, azimuthal averages, and streamwise fluxes. Most notably, we find that this transition causes significant increases in mixing near the pool surface, resulting in changes to each of these statistics. Additionally, we connect the non-dimensional parameters that dictate the transition to turbulence in the present reacting plumes and in inert helium plumes.

CRediT authorship contribution statement

Michael A. Meehan: Conceptualization, Performed simulations, Analyzed results, Created visualizations, Writing – original draft. **John C. Hewson:** Assisted with analyzing results, Assisted in writing paper. **Peter E. Hamlington:** Supervised research, Acquired funding and computing resources, Assisted in interpretation of results, Final review and editing.

Declaration of competing interest

The authors declare that they have no known competing financial interests or personal relationships that could have appeared to influence the work reported in this paper.

Acknowledgments

This article has been authored by an employee of National Technology and Engineering Solutions of Sandia, LLC under Contract No. DE-NA0003525 with the U.S. Department of Energy (DOE). The employee owns all right, title, and interest in and to the article and is solely responsible for its contents. The United States Government retains and the publisher, by accepting the article for publication, acknowledges that the United States Government retains a non-exclusive, paid-up, irrevocable, world-wide license to publish or reproduce the published form of this article or allow others to do so, for United States Government purposes. The DOE will provide public access to these results of federally sponsored research in accordance with the DOE Public Access Plan https://www.energy.gov/doe-public-accessplan. This paper describes objective technical results and analysis. Any subjective views or opinions that might be expressed in the paper do not necessarily represent the views of the U.S. Department of Energy or the United States Government.

PEH also acknowledges support from NSF award 1847111 and SERDP project RC20-1382. Computations were completed on the Onyx supercomputer at the Engineer Research and Development Center.

References

- A. Brown, et al., Proceedings of the first workshop organized by the IAFSS Working Group on Measurement and Computation of Fire Phenomena (MaCFP), Fire Saf. J. 101 (2018) 1–17.
- [2] E. Weckman, A. Strong, Experimental investigation of the turbulence structure of medium-scale methanol pool fires, Combust. Flame 105 (3) (1996) 245–266.
- [3] S. Tieszen, et al., Experimental study of the flow field in and around a one meter diameter methane fire. Combust. Flame 129 (4) (2002) 378–391.
- [4] S. Tieszen, et al., Experimental study of the effect of fuel mass flux on a 1-m-diameter methane fire and comparison with a hydrogen fire, Combust. Flame 139 (1-2) (2004) 126-141.
- [5] V.F. Nicolette, et al., A Turbulence Model for Buoyant Flows Based on Vorticity Generation, Sandia Report SAND2005-6273, Sandia National Laboratories, 2005.
- [6] D. Livescu, et al., High-Reynolds number Rayleigh-Taylor turbulence, J. Turbul. 10 (2009) N13.
- [7] C. Towery, et al., Spectral kinetic energy transfer in turbulent premixed reacting flows, Phys. Rev. E 93 (5) (2016) 053115.

- [8] A. Vali, et al., Transport phenomena within the liquid phase of a laboratory-scale circular methanol pool fire, Combust. Flame 161 (4) (2014) 1076–1084.
- [9] S.P. Domino, et al., Predicting large-scale pool fire dynamics using an unsteady flamelet-and large-eddy simulation-based model suite, Phys. Fluids 33 (8) (2021).
- [10] N.T. Wimer, et al., Numerical simulations of buoyancy-driven flows using adaptive mesh refinement: structure and dynamics of a large-scale helium plume, Theor. Comput. Fluid Dvn. 35 (2021) 61–91.
- [11] S.N. Scott, S.P. Domino, A computational examination of large-scale pool fires: variations in crosswind velocity and pool shape, Flow 2 (2022) E32.
- [12] G. Maragkos, et al., Towards predictive simulations of gaseous pool fires, Proc. Combust. Inst. 37 (3) (2019) 3927–3934.
- [13] J. Bell, et al., Active control for statistically stationary turbulent premixed flame simulations, Commun. Appl. Math. Comput. Sci. 1 (1) (2007) 29-51.
- [14] J.B. Bell, et al., Numerical simulation of a laboratory-scale turbulent slot flame, Proc. Combust. Inst. 31 (1) (2007) 1299–1307.
- [15] G. Maragkos, et al., Analysis of adaptive mesh refinement in a turbulent buoyant helium plume. Internat. J. Numer. Methods Fluids 94 (9) (2022) 1398–1415.
- [16] C. Lapointe, et al., Efficient simulations of propagating flames and fire suppression optimization using adaptive mesh refinement, Fluids 6 (9) (2021) 323.
- [17] B. Wu, et al., Detailed modeling of a small-scale turbulent pool fire, Combust. Flame 214 (2020) 224–237.
- [18] M.A. Meehan, N.T. Wimer, P.E. Hamlington, Richardson and Reynolds number effects on the near field of buoyant plumes: temporal variability and puffing, J. Fluid Mech. 950 (2022) A24.
- [19] M.A. Meehan, P.E. Hamlington, Richardson and Reynolds number effects on the near field of buoyant plumes: flow statistics and fluxes, J. Fluid Mech. 961 (2023) A7.
- [20] P.A. Durbin, Some recent developments in turbulence closure modeling, Annu. Rev. Fluid Mech. 50 (2018) 77–103
- [21] L. Esclapez, et al., PeleLMeX: an AMR low mach number reactive flow simulation code without level sub-cycling, J. Open Source Softw. 8 (90) (2023) 5450.
- [22] W. Zhang, et al., AMReX: a framework for block-structured adaptive mesh refinement, J. Open Source Softw. 4 (37) (2019) 1370.
- [23] M. Frenklach, et al., Optimization and analysis of large chemical kinetic mechanisms using the solution mapping method—combustion of methane, Prog. Energy Combust. Sci. 18 (1) (1992) 47–73.
- [24] C.J. Sung, et al., Further validation of an augmented reduced mechanism for methane oxidation: comparison of global parameters and detailed structure, Combust. Sci. Technol. 156 (1) (2000) 201–220.
- [25] M.S. Day, J.B. Bell, Numerical simulation of laminar reacting flows with complex chemistry, Combust. Theory Model, 4 (4) (2000) 535.
- [26] P.E. Hamlington, et al., Intermittency in premixed turbulent reacting flows, Phys. Fluids 24 (7) (2012).
- [27] P. Pagni, Pool fire vortex shedding frequencies, Appl. Mech. Rev. 43 (8) (1990) 166.
- [28] N. Yoshihara, A. Ito, H. Torikai, Flame characteristics of small-scale pool fires under low gravity environments, Proc. Combust. Inst. 34 (2) (2013) 2599–2606.
- 29] B.M. Cetegen, T.A. Ahmed, Experiments on the periodic instability of buoyant plumes and pool fires, Combust. Flame 93 (1–2) (1993) 157–184.
- [30] E. Zukoski, et al., Visible structure of buoyant diffusion flames, Symp. Int. Combust. 20 (1985) 361–366.
- [31] T. Ma, J. Quintiere, Numerical simulation of axi-symmetric fire plumes: accuracy and limitations, Fire Saf. J. 38 (5) (2003) 467–492.
- [32] G. Heskestad, A reduced-scale mass fire experiment, Combust. Flame 83 (3-4) (1991) 293-301.
- [33] M.A. Delichatsios, Air entrainment into buoyant jet flames and pool fires, Combust. Flame 70 (1) (1987) 33–46.
- [34] F.R. Menter, et al., Transition modelling for general purpose CFD codes, Flow Turbul. Combust. 77 (2006) 277–303.
- [35] T. Sayadi, P. Moin, Large eddy simulation of controlled transition to turbulence, Phys. Fluids 24 (11) (2012).